Research Article | Vol. 29, No. 2 / 18 January 2021 / Optics Express 974
Optics EXPRESS

Tunable fiber Fabry-Perot cavities with high passive stability

CARLOS SAAVEDRA,[1,2,3] DEEPAK PANDEY,[1,4] WOLFGANG ALT,[1] HANNES PFEIFER,[1] AND DIETER MESCHEDE[1]

[1]Institut für Angewandte Physik, Universität Bonn, Wegelerstr. 8, 53115 Bonn, Germany
[2]División de Ciencias e Ingenierías, Universidad de Guanajuato, 37150, Mexico
[3]carlos.salazar@iap.uni-bonn.de
[4]d.pandey@iap.uni-bonn.de
http://quantum-technologies.iap.uni-bonn.de/

Abstract: We present three high finesse tunable monolithic fiber Fabry-Perot cavities (FFPCs) with high passive mechanical stability. The fiber mirrors are fixed inside slotted glass ferrules, which guarantee an inherent alignment of the resonators. An attached piezoelectric element enables fast tuning of the FFPC resonance frequency over the entire free-spectral range for two of the designs. Stable locking of the cavity resonance is achieved for sub-Hertz feedback bandwidths, demonstrating the high passive stability. At the other limit, locking bandwidths up to tens of kilohertz, close to the first mechanical resonance, can be obtained. The root-mean-square frequency fluctuations are suppressed down to ~2% of the cavity linewidth. Over a wide frequency range, the frequency noise is dominated by the thermal noise limit of the system's mechanical resonances. The demonstrated small footprint devices can be used advantageously in a broad range of applications like cavity-based sensing techniques, optical filters or quantum light-matter interfaces.

1. Introduction

Miniaturized Fabry-Perot cavities are based on mirrors that are directly fabricated onto the end facets of optical fibers. They have emerged as a versatile optical resonator platform during the last decade [1,2]. They can provide small mode-volumes for high field concentrations in order to enhance light-matter interaction, while at the same time being inherently fiber coupled. Hence, they have quickly evolved into a standard platform to optically interface quantum emitters like atoms [3–6], ions [7,8], molecules [9], and solid state systems like quantum dots [10] or NV-centers [11]. Furthermore, they have been successfully used in cavity-optomechanical experiments involving a membrane inside the fiber Fabry-Perot cavity (FFPC) [12], for sensing of strain [13] and vibration [14], for cavity-enhanced microscopy [15], and they have been proposed as a fiber-coupled system for optical filtering [16].

The fiber mirrors that constitute an FFPC are created by laser ablation and a subsequent high-reflective coating of the end-facets of an optical fiber [1,17]. Assembling an FFPC typically requires an iterative adjustment of the two opposing fiber mirrors, using three translation and two angular degrees of freedom, to achieve optimal cavity alignment [1,18]. In order to control cavity birefringence also rotary adjustment of the fibers is needed [17,19]. After alignment, the fibers are glued to their respective holders, e.g. v-grooves. These are mounted on piezo-electric elements, attached to a common base, to enable tuning of the cavity resonance [2,18].

Such conventional FFPC realizations easily pick up low frequency acoustic noise due to the large distance of the fibers from the common base. Moreover, fiber tips protruding beyond their holders into the free space introduce additional noise due to bending modes. In order to stabilize these cavity systems an electronic locking scheme with feedback bandwidths of the order of several tens of kHz is required [2,20,21]. An alternative implementation, where the fiber mirrors

#412273 https://doi.org/10.1364/OE.412273
Journal © 2021 Received 12 Oct 2020; accepted 3 Dec 2020; published 5 Jan 2021

Optics EXPRESS

are fixed inside a common glass ferrule, was demonstrated in [2]. This reduces the complexity of the assembling process and at the same time increases the passive stability. The monolithic FFPC in [2], however, had a small scan range via slow thermal tuning only, and hence was limited in its applicability.

Here we present the fabrication, characterization of optical properties, and locking characteristics of three monolithic FFPCs. The FFPC devices use slotted glass ferrules glued to a piezoelectric element for fast scanning over the entire free-spectral range of the resonators. The fiber mirrors are inherently aligned by the guide provided from the glass ferrule. Due to the high passive stability, feedback bandwidths as low as 20 mHz are sufficient to lock the cavity resonance to an external laser under laboratory conditions. Fast piezo tuning allows for feedback bandwidths up to 27 kHz for tight stabilization of the cavity resonance.

2. FFPC design and fabrication

In Fig. 1 we show the geometry of three FFPC devices based on glass ferrules. These commercially available ferrules (8 mm × 1.25 mm × 1.25 mm) are made out of fused silica with 131 μm nominal inner diameter of the bore. The different slotting patterns of the ferrules are cut using a diamond-plated wire saw. Complete slots are finished only after gluing the ferrule onto the piezo-element to maintain the precise alignment of the bores of the segmented blocks (details see Supplement 1 Sec. 1). The electrodes of the piezo-element are connected to copper wires by means of a conductive glue.

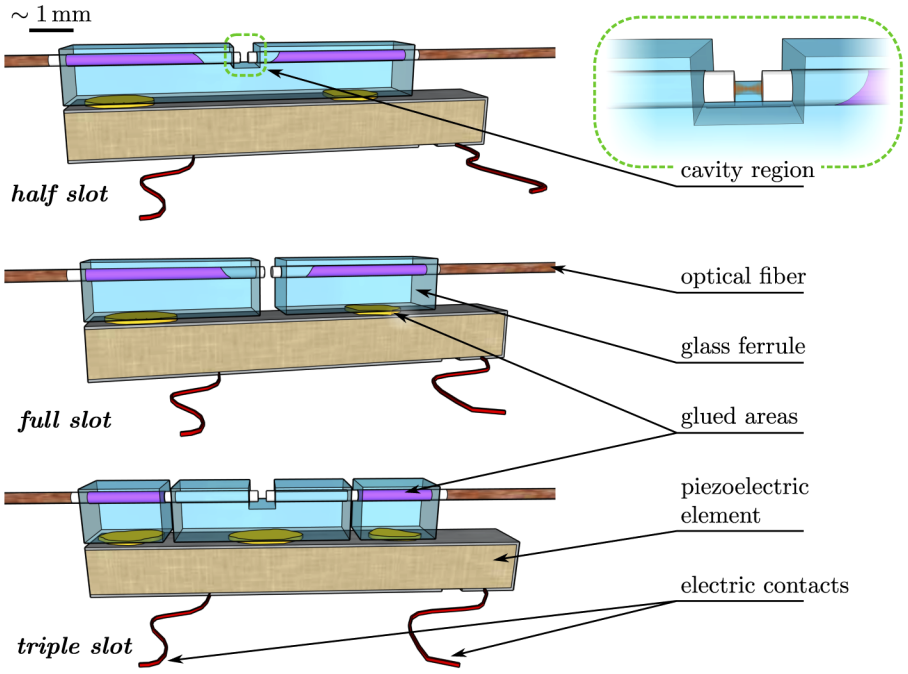

Fig. 1. Designs and components of the three FFPCs. The optical cavities are formed by concave dielectric mirrors on the opposing end-facets of the optical fibers (diameters exaggerated by a factor of 2) at the center of the structures. The fibers are glued into the glass ferrules, which are in turn glued to piezoelectric elements for tuning the cavity resonances.

In the next step, the optical cavity is formed by inserting the fiber mirrors into the ferrule. The opposing end facets are placed at the center area of the ferrule to form a cavity with length L_{cavity} according to the desired free spectral range $\nu_{\text{FSR}} = c/2\,L_{\text{cavity}}$ with c the speed of light. In the

Optics EXPRESS

half and triple slot FFPC the central slot does not fully cut through the bore of the ferrule, such that the fiber tips rest at the base of the bore as shown in the inset of Fig. 1. In the full slot design, the slotting gap is kept narrow ($\approx$ 250 μm) such that there is only a small protrusion of the fiber tips into the free space. This constrains the bending motion of the fiber tips.

To find the optical resonance of the cavity, one of the fiber mirrors is scanned using a piezo-driven translation stage while observing the cavity reflection of an incident probe laser. The birefringence of the cavity, due to ellipticity of the mirrors, is reduced by rotating one of the fibers about the cavity axis [19]. The guide provided by the ferrule significantly simplifies the cavity alignment by requiring only one translation and one rotation degree of freedom, as long as the used fiber mirrors only show small decentrations from the fiber axis. In the last step, the fibers are glued into the ferrule, while keeping the cavity approximately resonant with a laser at the target wavelength. A small amount of UV-curable glue is applied to the fiber where it enters the ferrule. Capillary forces let the glue flow into the space between fiber and ferrule wall, where it is subsequently hardened by UV-light illumination.

The piezo-element is a rectangular ceramic block of dimensions 10 mm $\times$ 1 mm $\times$ 1 mm such that it fits the ferrule (Fig. 1). Applying a voltage to the piezo-element causes a longitudinal displacement of the fiber end facets with respect to each other. The resulting length change ΔL_{cavity}, tunes the optical resonance frequencies ($\Delta\nu_{\text{scan}} = 2\,\nu_{\text{FSR}}\,\Delta L_{\text{cavity}}/\lambda$). For fully slotted designs, the tuning range depends on the spacing of the glue points on the piezo element and the length tuning is approximately given by the expansion of the unloaded piezo-element between the glue points. The distance between relevant glue contact points for the full (triple) slot design is $\approx$ 2.7 mm (7.4 mm), translating into a length variation of $\Delta L_{\text{cavity}} \approx 0.5$ μm (1.5 μm) for a 1 kV_{pp} piezo voltage range. The half slot design shows the smallest tuning range since the length change of the cavity is mediated by the elastic deformation of the stiff ferrule. The measured tuning ranges for the three FFPCs are listed in Table 1.

Table 1. Overview of the optical and locking characteristics of the three FFPCs

Property	Half slot FFPC	Full slot FFPC	Triple slot FFPC
Finesse	93000	61000	99000
Linewidth (FWHM)	17 MHz	27 MHz	16 MHz
FSR	1.61 THz	1.62 THz	1.61 THz
Scan range[a]	0.13 THz	2.27 THz	6.10 THz
Max. locking bandwidth	20 kHz	25 kHz	27 kHz
Mechanical resonance[b]	56 kHz	34 kHz	32 kHz
Min. locking bandwidth	20 mHz	65 mHz	110 mHz
Locked freq. noise (rms)[c]	0.37 MHz	0.40 MHz	0.64 MHz

[a] 1 kV_{pp}
[b] Lowest frequency mode
[c] Integrated for 10 Hz – 1 MHz

3. Optical characterization

For the characterization of the completed FFPCs, the light from a 780 nm narrow linewidth ($\sim$ 200 kHz) laser is sent through an electro-optic modulator (EOM) that is driven at 250 MHz to add sidebands to the laser carrier frequency (see Fig. 2). A combination of half- and quarter-wave plates is used to control the polarization state of the light before being coupled into the optical fiber that leads to the FFPC. The reflected (transmitted) light from the cavity is directed onto a photodiode $\text{PD}_{\text{reflected}}$ ($\text{PD}_{\text{transmitted}}$). The cavity length is scanned by driving the piezo-element.

Optics EXPRESS

To measure the cavity linewidth, the EOM-generated sidebands are used as frequency markers (see inset in Fig. 2).

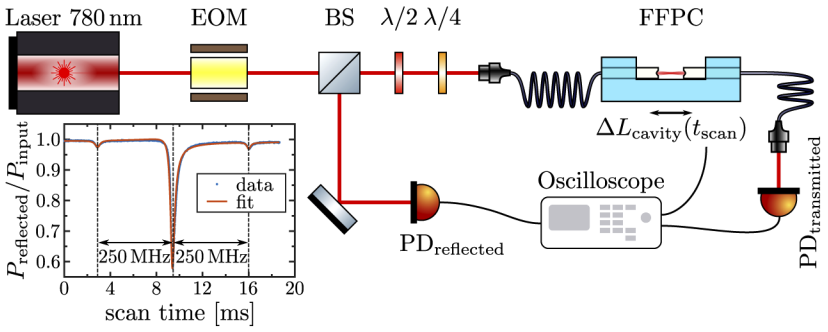

Fig. 2. Setup for characterizing FFPCs. The reflected and transmitted laser light power from the FFPC is monitored by the two photodiodes (PD) while the FFPC length L_{cavity} is scanned. The waveplates ($\lambda/2$ and $\lambda/4$) before the input fiber are used to investigate the polarization mode splitting of the cavity. The calibration of scan time t_{scan} to frequency is achieved by modulating sidebands onto the laser tone using an electro-optic modulator (EOM). BS represents a non-polarizing beam splitter. (sketch uses [22])

The fiber mirrors used here have a transmission of $T \approx$ 15 ppm and absorption of $A \approx$ 25 ppm of the dielectric mirror coating. The concave mirror shape on the fiber end facet was created via CO_2-laser ablation with a radius of curvature of $\approx$ 180 μm. To experimentally determine the linewith and finesse of the FFPCs, the measured reflection signal is fitted using a sum of a Lorentzian and its corresponding dispersive function [2,23] as shown in Fig. 3(a). In this example of the half slot FFPC, the free spectral range of the 93 μm long cavity is $\nu_{\text{FSR}} = c/2L_{\text{cavity}} \sim$ 1.61 THz yielding a maximum Finesse of $\mathcal{F} \approx 93 \times 10^3$ from the extracted linewidth of $\kappa/2\pi = (17.34 \pm 0.014)$ MHz. The finesse, the FSR and the linewidths for the three FFPCs are listed in Table 1. While the half slot FFPC shows a moderate tunability of 0.13 GHz/V due to the stiff ferrule geometry, the full and triple slot FFPCs exhibit large tunabilities of 2.27 GHz/V and 6.1 GHz/V respectively, enabling full FSR scans at moderate voltages as shown in Fig. 3 b.

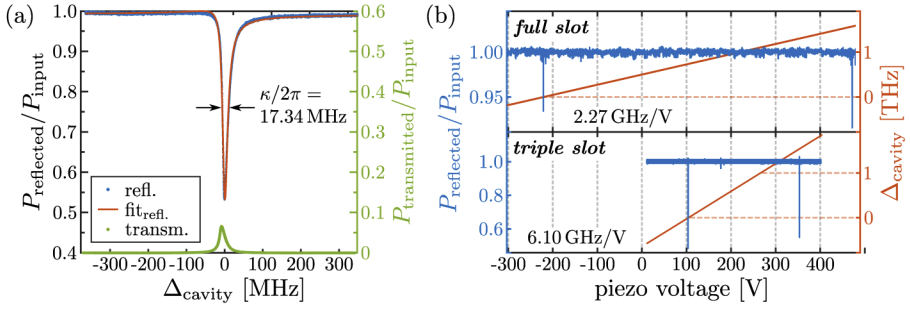

Fig. 3. (a) Reflected and transmitted power fraction in an exemplary cavity scan of the half slot FFPC with Lorentzian and dispersive fit [2]. (b) Scan of the full free spectral range (FSR) for full slot and triple slots FFPCs. Detailed FFPC properties are listed in Table 1.

Apart from the piezo-electric tuning, the optical cavity resonance is also sensitive to the ambient temperature [2], which can be used for tuning by $\approx$ 8 Gz/K (Supplement 1 Sec. 5).

Optics EXPRESS

4. Cavity locking

The passive and active stability for the three FFPCs is analysed by investigating the closed-loop locking characteristics, where locking refers to an active stabilization of a cavity resonance to a narrow linewidth (~ 200 kHz) laser. We use the standard Pound-Drever-Hall (PDH) locking technique [24], using the EOM-generated sidebands. The schematic of the locking setup is shown in Fig. 4(a). The PDH error-signal e is retrieved from the rf mixer by down-converting the output of the photodiode signal r with the 250 MHz reference signal. The error signal is fed into a PI-controller which drives the piezo attached to the cavity assembly. The PI-controller consists of a variable-gain proportional (P) and an integrator (I) control system. The output of the PI-controller can optionally be low-pass filtered by adding a resistor in series with the piezo.

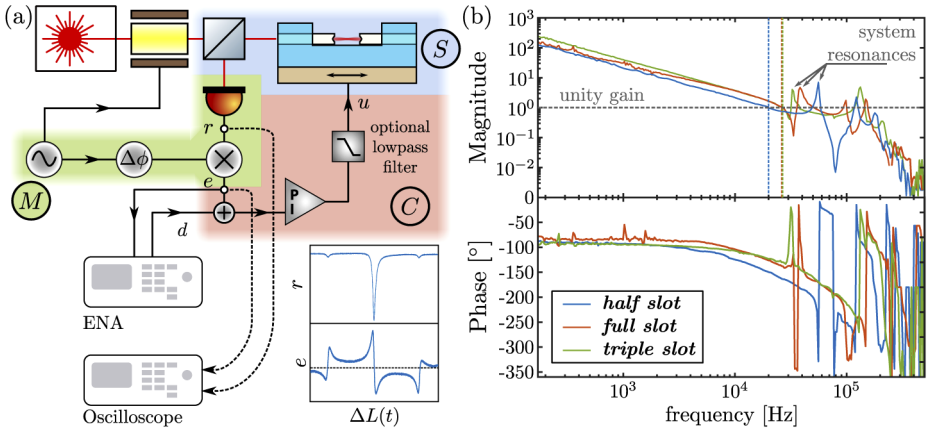

Fig. 4. (a) Schematic of the PDH-locking setup for investigating the feedback bandwidth and stability of monolithic FFPCs. The closed feedback system consists of the FFPC device (S), the PDH mixer setup (M), and the feedback controller (C). The input to the PI-controller is the PDH error signal e. The output voltage u is applied to the piezo. The gain of the PI-controller can be adjusted to explore different locking bandwidths. To measure the frequency response of the closed-loop circuit a frequency sweep signal d from the electrical network analyser (ENA) can be added to e. (b) The plots show the magnitude and phase of the full system (CSM) transfer function for the maximum achieved bandwidths (dash-dotted vertical lines) of the three designs listed in Table 1. Sketch uses [22].

We analyse the locking performance of the FFPCs based on techniques used in [20,25]. The frequency-dependent gains (transfer functions) of the components in the servo-loop, as depicted in Fig. 4(a), are: C - the PI-controller including the optional low pass filter, S - the cavity-assembly, and M - the measurement setup consisting of photodiode and mixer. To retrieve the loop gain $CSM(\nu)$, an electronic network analyzer (ENA) is used to add a frequency-swept external disturbance d to the input of the PI-controller, while the error signal is monitored.

The loop gain $CSM(\nu)$ is deduced from the measured closed-loop response of the error signal as follows

$$CSM(\nu) = -\frac{A}{A+1}, \; A = \frac{e}{d}. \tag{1}$$

We directly obtain A from the network analyzer by monitoring the spectrum of the error signal e (Fig. 4(a)). The closed-loop locking bandwidth (LBW) is given by the unity-gain frequency, i.e the lowest frequency for which $|CSM(\nu)| = 1$. This frequency is the upper limit at which the PI-controller can exert an effective feedback against cavity resonance drifts. By changing the gain settings of the PI-controller, this frequency can be adjusted in order to realize different locking bandwidths.

Optics EXPRESS

4.1. Maximum locking bandwidth

To find the maximum achievable LBW of the FFPC devices, the I-gain of the PI-controller is set to the highest value which allows for stable locking. As shown in Fig. 4(b), the maximum LBWs for all three FFPCs are a few tens of kHz, limited by mechanical resonances of the FFPC assembly (details Sect. 4.4). The rms frequency fluctuation for the maximum LBW is similar to the one given in Table 1.

4.2. Stability of the FFPCs

For quantitatively characterizing the high passive stability, we extract a value for the minimum locking bandwidth of the FFPCs. For this purpose, the I-gain of the PI-controller is set to the lowest possible value which still allows a stable cavity locking. We found that all three cavities can be locked for many hours under laboratory conditions without any acoustic isolation even for LBW at sub-Hertz level. Figure 5(a) shows the plots of $|CSM(\nu)|$ vs frequency at the lowest gain setting. The LBW is extracted from the intersection of the extrapolated loop gain with the unity gain line. The extracted minimum LBWs for the three FFPCs are given in Table 1, with the lowest measured value of 20 mHz for the half slot FFPC. As more slots are introduced for achieving larger tunability, the value of the lowest LBW increases successively for full slot and triple slot FFPCs. Therefore, the larger tunability of the FFPC is obtained at the cost of a slight reduction of the stability. This is further characterised by the frequency noise spectrum for a locked FFPC as described below.

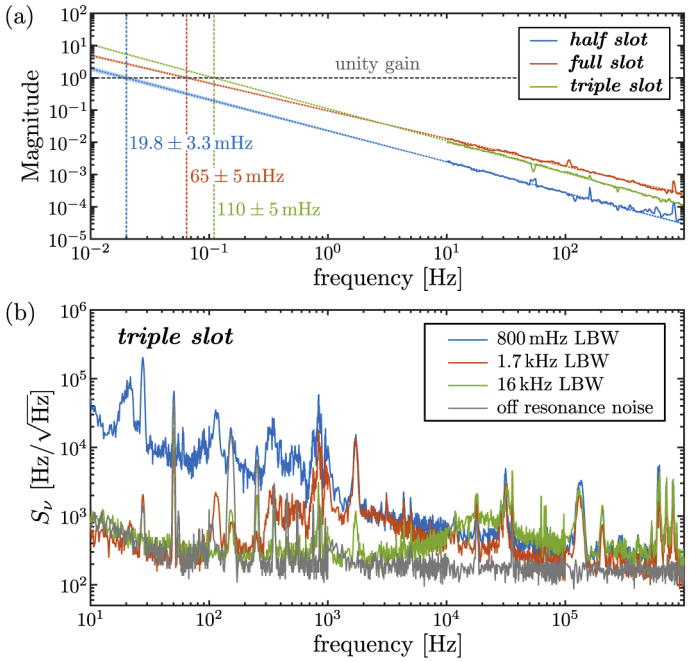

Fig. 5. (a) Magnitude of the closed-loop-gain ($CSM(\nu)$) for the three FFPCs with small locking bandwidths (LBW). The intersections of the measured transfer functions with the unity gain line are the values corresponding to the low LBW. (b) Measurements of the frequency noise spectral density S_ν for the triple slot FFPC for three different LBWs. The off resonance noise curve corresponds to the detection noise limit, measured when the cavity is unlocked and far-off resonance.

Optics EXPRESS

4.3. Noise-spectral-density analysis

To compare the noise characteristics of the FFPCs under different lock conditions, we measure their frequency noise spectral densities (S_ν), which are derived from the measured noise spectral densities of the error signals. Figure 5(b) shows S_ν for the triple slot FFPC at three different locking bandwidths (see Supplement 1 Sec. 3 for the other two FFPCs). The integrated rms frequency noise from these measurements amounts to $\nu_{\mathrm{rms}} = (1.19, 0.64, 1.28, 0.24)$ MHz for the 800 mHz, 1.7 kHz, 16 kHz locking bandwidths and the off resonance noise respectively. The off resonance noise is measured with an unlocked cavity far away from resonance. Although the locking bandwidth is changed by almost four orders of magnitude, the value of the integrated rms frequency noise remains similar, demonstrating the inherent high passive stability of the FFPCs. The slightly higher noise for sub-Hertz locking bandwidth is due to the uncompensated environmental acoustic noise below 1 kHz, while at a LBW of 1.7 kHz acoustic noise is suppressed. We have also observed that when the locking bandwidth approaches the mechanical resonances, the rms frequency noise increases again due to the excitation of these resonances.

4.4. Mechanical resonances

The most prominent contribution to the measured frequency noise at higher frequencies is caused by the mechanical resonances of the assemblies starting around 30 kHz, see Fig. 5 and Table 1.

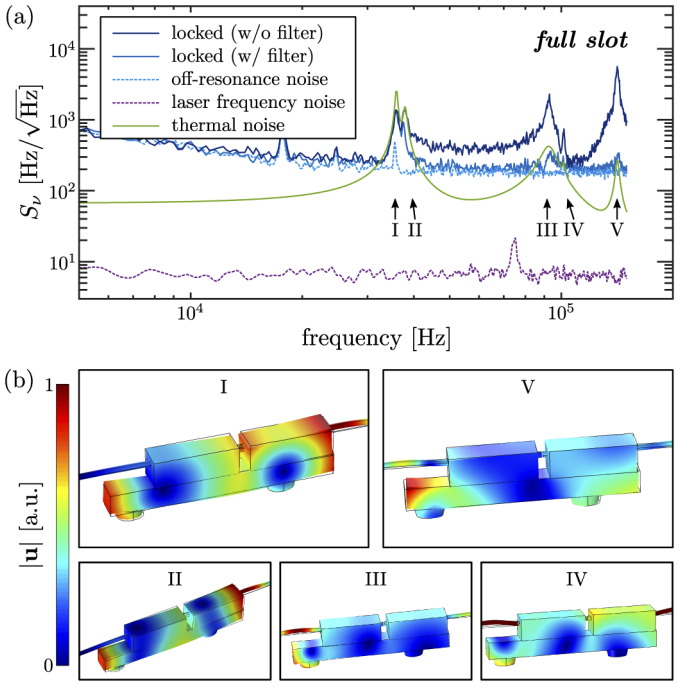

Fig. 6. Analysis of the measured FFPC frequency noise induced by mechanical resonances of the system for the full slot FFPC. (a) The measured S_ν are compared with the laser frequency noise and with the expected noise from thermally excited mechanical resonances of the system. The S_ν approaches the expected thermal noise limit near the mechanical resonances. Without a low-pass filter, excess electrical noise is coupled to the cavity through the piezoelectric element for some of the modes. (b) Displacement fields of the mechanical resonances included in the model. The two most prominent resonances, I and V, correspond to a bending mode (no piezoelectric coupling) and a longitudinal stretching mode (piezoelectrically coupled) of the structure.

Optics EXPRESS

Without active damping of these resonances, the minimum achievable noise corresponds to the thermal excitation of these modes at ambient temperature.

In order to quantify the thermal noise limit, we performed finite element simulations [26] of the assembly geometries (see Supplement 1 Sec. 4). These are used to extract the displacement fields of the mechanical eigenmodes, their effective masses and optomechanical coupling strengths. Damping was not included in the simulations. The resonances in the recorded noise spectral densities are then attributed to eigenmodes found in the simulation appearing at close-by frequencies. The thermal excitation of the mechanical resonances is calculated from the fluctuation-dissipation theorem using the fitted frequencies and linewidths that parametrize the damping of the modes. Together with the simulated parameters the expected signal in the frequency noise spectrum [27] can be compared to the measured frequency noise spectral density. An example for this is shown in Fig. 6(a) for the full slot FFPC. Here, we find five mechanical modes (I-V in Fig. 6(b)) with substantial coupling to the optical resonance for frequencies up to 150 kHz. The two most prominent modes in the experiment (blue traces), I and V, correspond to a bending and longitudinal stretching motion of the piezo. The calculated thermally induced frequency noise is shown in green in Fig. 6(a). Since the stretching of the piezo is coupled to the driving voltage by the piezoelectric effect, excess electrical noise from the controller is resonantly coupled to the system at the stretching mode frequency (dark blue curve in Fig. 6(a)). The excess electrical noise can however be removed by inserting a suitable low pass filter before the piezo (medium blue curve). After inserting the filter, the measured noise is compatible with the theoretically achievable thermal noise limit and the off-resonance detection noise (dashed light blue curve). The frequency noise of the laser does not play a role since it is found to be more than an order of magnitude lower than the detection noise (see Supplement 1 Sec. 2).

5. Conclusion

In this paper we have demonstrated a versatile, robust and simple approach for building stable fiber Fabry-Perot cavities with wide frequency tunability and simultaneous high passive stability. The demonstrated high locking bandwidth is possible due to the first mechanical resonance frequencies of the monolithic devices occurring only above tens of kHz. Achieving stable locking at tens of mHz feedback bandwidth, which implies that the cavity resonance is stable on a minute time scale, and reaching the thermal noise limit at higher frequencies, proves the high passive stability of these devices against slow and fast environmental disturbances. These compact and inherently fiber coupled cavities can be readily implemented in various applications like cavity-based spectroscopy of gases, tunable optical filters, and cavity quantum electrodynamics experiments, which all benefit from highly stable optical resonators.

By incorporating mode-matched [28] and millimeters long FFPCs [16] in our compact devices, stable resonators with linewidths below 1 MHz can be achieved. This will enable the realization of compact gas sensors for airborne applications as well as miniaturized cavity enhanced vapor based light-matter interfaces. Considering ferrules made of ultra-low expansion glass or with cryogenically cooled FFPCs, one can envision miniaturized and portable optical oscillators with high short term stability.

Funding. Deutsche Forschungsgemeinschaft (EXC 2004/1 – 390534769); Consejo Nacional de Ciencia y Tecnología; Bundesministerium für Bildung und Forschung (Q.Link.X and FaResQ).

Acknowledgements. The authors thank Stephan Kucera for valuable discussions. This work was supported by the Bundesministerium für Bildung und Forschung (BMBF), projects Q.Link.X and FaResQ. C.S. is supported by a national scholarship from CONACYT, México. W.A. acknowledges funding by the Deutsche Forschungsgemeinschaft (DFG, German Research Foundation) under Germany's Excellence Strategy – Cluster of Excellence Matter and Light for Quantum Computing (ML4Q) EXC 2004/1 – 390534769.

Disclosures. The authors declare no conflicts of interest.

See Supplement 1 for supporting content.

Optics EXPRESS

References

1. D. Hunger, T. Steinmetz, Y. Colombe, C. Deutsch, T. W. Hänsch, and J. Reichel, "A fiber fabry–perot cavity with high finesse," New J. Phys. **12**(6), 065038 (2010).
2. J. Gallego, S. Ghosh, S. K. Alavi, W. Alt, M. Martinez-Dorantes, D. Meschede, and L. Ratschbacher, "High-finesse fiber fabry–perot cavities: stabilization and mode matching analysis," Appl. Phys. B **122**(3), 47 (2016).
3. J. Gallego, W. Alt, T. Macha, M. Martinez-Dorantes, D. Pandey, and D. Meschede, "Strong purcell effect on a neutral atom trapped in an open fiber cavity," Phys. Rev. Lett. **121**(17), 173603 (2018).
4. Y. Colombe, T. Steinmetz, G. Dubois, F. Linke, D. Hunger, and J. Reichel, "Strong atom–field coupling for bose–einstein condensates in an optical cavity on a chip," Nature **450**(7167), 272–276 (2007).
5. T. Macha, E. Urunuela, W. Alt, M. Ammenwerth, D. Pandey, H. Pfeifer, and D. Meschede, "Nonadiabatic storage of short light pulses in an atom-cavity system," Phys. Rev. A **101**(5), 053406 (2020).
6. M. Brekenfeld, D. Niemietz, J. D. Christesen, and G. Rempe, "A quantum network node with crossed optical fibre cavities," Nat. Phys. **16**(6), 647–651 (2020).
7. M. Steiner, H. M. Meyer, C. Deutsch, J. Reichel, and M. Köhl, "Single ion coupled to an optical fiber cavity," Phys. Rev. Lett. **110**(4), 043003 (2013).
8. H. Takahashi, E. Kassa, C. Christoforou, and M. Keller, "Strong coupling of a single ion to an optical cavity," Phys. Rev. Lett. **124**(1), 013602 (2020).
9. C. Toninelli, Y. Delley, T. Stöferle, A. Renn, S. Götzinger, and V. Sandoghdar, "A scanning microcavity for in situ control of single-molecule emission," Appl. Phys. Lett. **97**(2), 021107 (2010).
10. J. Miguel-Sánchez, A. Reinhard, E. Togan, T. Volz, A. Imamoglu, B. Besga, J. Reichel, and J. Estève, "Cavity quantum electrodynamics with charge-controlled quantum dots coupled to a fiber fabry–perot cavity," New J. Phys. **15**(4), 045002 (2013).
11. R. Albrecht, A. Bommer, C. Deutsch, J. Reichel, and C. Becher, "Coupling of a single nitrogen-vacancy center in diamond to a fiber-based microcavity," Phys. Rev. Lett. **110**(24), 243602 (2013).
12. N. Flowers-Jacobs, S. Hoch, J. Sankey, A. Kashkanova, A. Jayich, C. Deutsch, J. Reichel, and J. Harris, "Fiber-cavity-based optomechanical device," Appl. Phys. Lett. **101**(22), 221109 (2012).
13. M. Jiang and E. Gerhard, "A simple strain sensor using a thin film as a low-finesse fiber-optic fabry–perot interferometer," Sens. Actuators, A **88**(1), 41–46 (2001).
14. Y. R. García, J. M. Corres, and J. Goicoechea, "Vibration detection using optical fiber sensors," J. Sens. **2010**, 1–12 (2010).
15. M. Mader, J. Reichel, T. W. Hänsch, and D. Hunger, "A scanning cavity microscope," Nat. Commun. **6**(1), 7249 (2015).
16. K. Ott, S. Garcia, R. Kohlhaas, K. Schüppert, P. Rosenbusch, R. Long, and J. Reichel, "Millimeter-long fiber fabry-perot cavities," Opt. Express **24**(9), 9839–9853 (2016).
17. M. Uphoff, M. Brekenfeld, G. Rempe, and S. Ritter, "Frequency splitting of polarization eigenmodes in microscopic fabry–perot cavities," New J. Phys. **17**(1), 013053 (2015).
18. B. Brandstätter, A. McClung, K. Schüppert, B. Casabone, K. Friebe, A. Stute, P. O. Schmidt, C. Deutsch, J. Reichel, and R. Blatt, "Integrated fiber-mirror ion trap for strong ion-cavity coupling," Rev. Sci. Instrum. **84**(12), 123104 (2013).
19. S. Garcia, F. Ferri, K. Ott, J. Reichel, and R. Long, "Dual-wavelength fiber fabry-perot cavities with engineered birefringence," Opt. Express **26**(17), 22249–22263 (2018).
20. E. Janitz, M. Ruf, Y. Fontana, J. Sankey, and L. Childress, "High mechanical bandwidth fiber-coupled fabry-perot cavity," Opt. Express **25**(17), 20932–20943 (2017).
21. J. F. Brachmann, H. Kaupp, T. W. Hänsch, and D. Hunger, "Photothermal effects in ultra-precisely stabilized tunable microcavities," Opt. Express **24**(18), 21205–21215 (2016).
22. A. Franzen, "ComponentLibrary," Licensed under CC BY-NC 3.0, http://www.gwoptics.org/ComponentLibrary/.
23. A. Bick, C. Staarmann, P. Christoph, O. Hellmig, J. Heinze, K. Sengstock, and C. Becker, "The role of mode match in fiber cavities," Rev. Sci. Instrum. **87**(1), 013102 (2016).
24. R. Drever, J. L. Hall, F. Kowalski, J. Hough, G. Ford, A. Munley, and H. Ward, "Laser phase and frequency stabilization using an optical resonator," Appl. Phys. B **31**(2), 97–105 (1983).
25. C. Reinhardt, T. Müller, and J. C. Sankey, "Simple delay-limited sideband locking with heterodyne readout," Opt. Express **25**(2), 1582–1597 (2017).
26. COMSOL AB, C. Reinhardt, "AB COMSOL Multiphysics® v. 5.2," www.comsol.com. Stockholm, Sweden.
27. M. Gorodetksy, A. Schliesser, G. Anetsberger, S. Deleglise, and T. J. Kippenberg, "Determination of the vacuum optomechanical coupling rate using frequency noise calibration," Opt. Express **18**(22), 23236–23246 (2010).
28. G. K. Gulati, H. Takahashi, N. Podoliak, P. Horak, and M. Keller, "Fiber cavities with integrated mode matching optics," Sci. Rep. **7**(1), 5556 (2017).

Supplemental Document

Optics EXPRESS

Tunable fiber Fabry-Perot cavities with high passive stability: supplement

CARLOS SAAVEDRA,[1,2,3] DEEPAK PANDEY,[1,4] WOLFGANG ALT,[1] HANNES PFEIFER,[1] AND DIETER MESCHEDE[1]

[1] *Institut für Angewandte Physik, Universität Bonn, Wegelerstr. 8, 53115 Bonn, Germany*
[2] *División de Ciencias e Ingenierías, Universidad de Guanajuato, 37150, Mexico*
[3] *carlos.salazar@iap.uni-bonn.de*
[4] *d.pandey@iap.uni-bonn.de*
http://quantum-technologies.iap.uni-bonn.de/

Supplement DOI: https://doi.org/10.6084/m9.figshare.13325579

Parent Article DOI: https://doi.org/10.1364/OE.412273

Tunable Fiber Fabry-Perot Cavities with High Passive Stability

CARLOS SAAVEDRA,[1,2,*] DEEPAK PANDEY,[1,†] WOLFGANG ALT,[1] HANNES PFEIFER[1] AND DIETER MESCHEDE[1]

[1] *Institut für Angewandte Physik, Universität Bonn, Wegelerstr. 8, 53115 Bonn, Germany*
[2] *División de Ciencias e Ingenierías, Universidad de Guanajuato, México*
[*] *carlos.salazar@iap.uni-bonn.de,* [†] *d.pandey@iap.uni-bonn.de*
http://quantum-technologies.iap.uni-bonn.de/

Abstract: In the following, we present details of the fabrication process for building the three FFPCs presented in the main manuscript. All components and materials are described such that the interested readers can easily reproduce these systems. Details about the measurement of the frequency noise spectral density are given for all three FFPCs. The methods for combining finite element simulations with the modeling of thermal noise of the FFPCs are described. At the end, the thermal tunability of the realized FFPCs is presented.

1. FFPC fabrication

Besides the fiber mirrors (see Sec. 3 main text), the important components for the demonstrated FFPCs include the glass ferrules, piezo-electric elements, glues and the electrical contact wires, which are specified below.

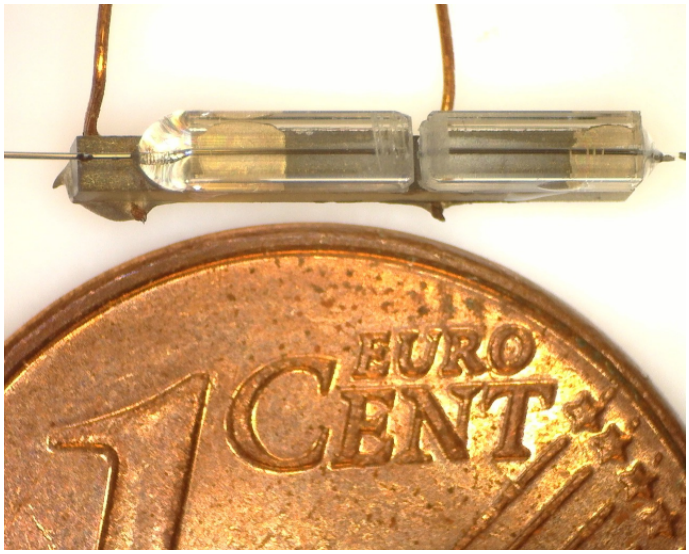

Fig. 1. Photograph of a full slot FFPC, a compact and miniaturized high finesse resonator with wide frequency tuning and high stability, and a 1 euro cent coin (for size comparison). The FFPC slotted region allows easy access to the cavity mode volume.

1.1. Piezo-ferrule assembly preparation

Piezo-electric element: The piezo-element is a 10 mm × 1 mm × 1 mm PIC151 ceramic (Model-no. 51638 from PI Ceramic GmbH), with relevant piezo modulus $d_{31} \approx -2 \times 10^{-10}\,\mathrm{C\,N^{-1}}$. The load-free expansion is specified to be $\Delta L_\mathrm{p} = d_{31} \cdot L_\mathrm{p} U / t_\mathrm{p}$, where U is the applied voltage, L_p the length and t_p the thickness of the piezo-element. The applicable voltage range for the used piezo-element is −400 V to 2 kV.
Ferrules: We used commercially available fused silica glass ferrules from VitroCom CFQ BLOCK FERRULE with 131 µm nominal inner bore diameter and a size of 8 mm × 1.25 mm × 1.25 mm.
Assembly preparation: As a first step towards preparing the assembly, the piezo electrodes are connected to vacuum compatible and kapton insulated copper wires (diameter 0.3 mm, 311-KAP-025, Allectra GmbH) by using a small amount of vacuum compatible conductive glue (two-components silver filled Epoxy, EPO-TEK® H20-E). For curing the glue, baking at 110 °C for 1 hour is required according to the data-sheet. In the next steps, the glass ferrules used for the FFPCs are slotted using a diamond-plated thin wire as shown in the Fig. 2 (a). For the half slot FFPC, the ferrule is sawed at the center until the partial section of the bore is reached. Following, the slotted ferrule is glued to the piezo-electric element using conductive glue and then thermally cured. Full cuts for the other two (full slot, triple slot) FFPCs are made by first slotting the ferrule at the desired full cut position up to the half of the ferrule height, Fig. 2 (a). The ferrules are then glued to the piezo with slots facing it as shown in the left part of Fig. 2 (b). Finally the full cuts are finished by slotting the ferrule from the top again such that the remaining glass at the already slotted positions is completely removed, Fig. 2 (c). To avoid damaging the fragile ferrule as well as to maintain the alignment of the bore, a careful sawing with small force is required.

The slotted ferrules are cleaned to remove residual particles from the bore using an iterative process of cleaning with high pressure air, followed by distilled water and acetone, and further using a bare fiber to remove trapped dust or particles from the bore of the ferrules.

1.2. Optical cavity fabrication

After the successful testing of the electrical contacts, the assembly is temporally fixed on an insulating base. Two high magnification USB-cameras (Dino-Lite digital microscope) are used to observe the ferrule bore and the central slot while inserting the fibers using translation stages. The distance between the two fiber mirrors is scanned using a piezo driven translation stage to observe the cavity resonance and thereby estimating the finesse and the coupling depths, where the coupling depth is defined as the ratio of the on-resonance versus off-resonance reflected light of a probe laser from the cavity. The dependence of these optical properties in relation to the length of the cavity is shown in Fig. 3. Although, the mirrors used in all FFPCs are expected to have the same transmission properties as mentioned in the main text, there are many factors which lead to slight differences in the optical properties (see main text Tab. 1) between the three FFPCs. These factors are , e.g., the decentration of the mirror with respect to the fiber, slightly different behaviour of the mirror transmission after annealing and possible contamination of the fiber mirrors during the assembling process.

The optical properties of the resonators also depend on the relative alignment of the two fiber mirrors. However, we observe that the cavity length adjustment using the guide provided by the ferrule maintains the resonator alignment and therefore the limitation of the achievable finesse is only due to the losses in the dielectric coating and due to the clipping of the beams on the fiber mirrors. The coupling depth, on the other hand, additionally depends on the mode matching between the fiber and the cavity mode. For the assembled FFPCs, we observe that the finesse before gluing the fibers is in most cases close to the one obtained after the mirrors are glued, Fig. 3.

Here we have used a cavity length of around 93 µm for the FFPCs. The fibers are glued using a

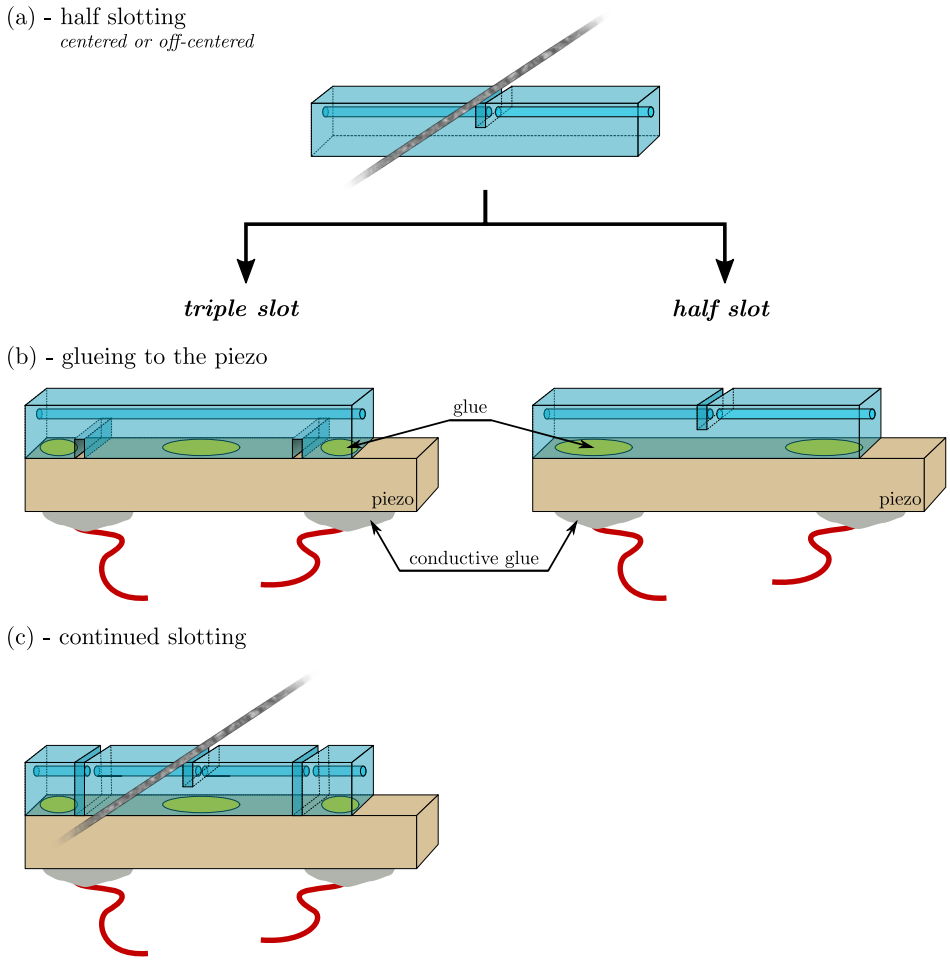

Fig. 2. Schematics for the piezo-ferrule assembly preparation. a) First, the ferrules are slotted at specific positions (depending upon the design choice) using a diamond-platted wire. b) The slotted ferrules are glued to the piezo-element. For the half slot FFPC, the assembly is ready at this point. c) Additional slotting is required for full slot and triple slot FFPCs.

low viscosity and vacuum compatible UV-curable glue (UV16, MasterBond®) as also described in the main text. The cavity length is adjusted close to the target resonance by observing the resonance peak while scanning the piezo and successively reducing the scan range. Once the UV-light is switched on, the scan is reduced to zero. We have observed that this procedure is good enough to keep the FFPC close to the target resonance while the glue hardens. For the full slot cavity (FSC) we have observed a degradation of the Finesse after gluing the mirrors (Fig. 3) which we believe is due to a contamination of the mirrors.

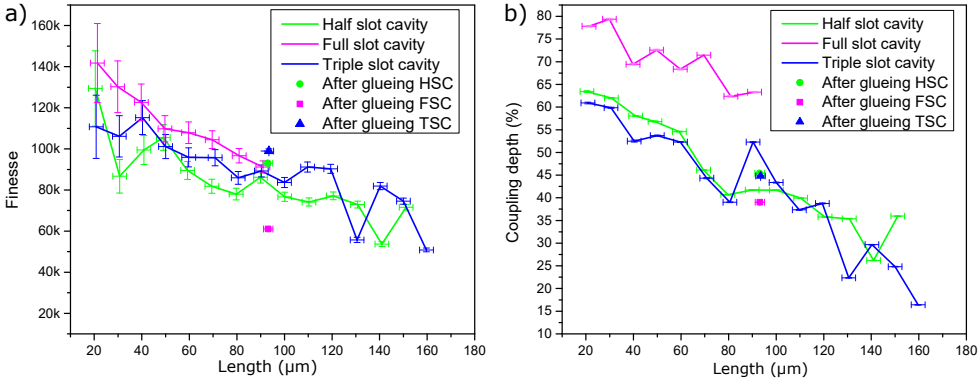

Fig. 3. Comparison of the optical properties of the three cavity designs before (line) and after (dot) gluing the fiber mirrors inside the ferrule bore. a) Finesse vs length, b) Coupling depth vs length for half slot cavity (HSC) , full slot cavity (FSC) and triple slot cavity (TSC).

2. Laser frequency noise

The linewidth and frequency noise of the laser is measured by using a linewidth analyser from HighFinesse®. For the unlocked laser, the measured linewidth ($\Delta\nu$) is 20 kHz $\leq \Delta\nu \leq$ 200 kHz with a typical value around 50 kHz. The measured laser frequency noise is shown in Fig. 4. These measurements confirms that the linewidth and the frequency noise of the laser are much smaller compared to the FFPC linewidth and the frequency noise of the locked cavity (see next section).

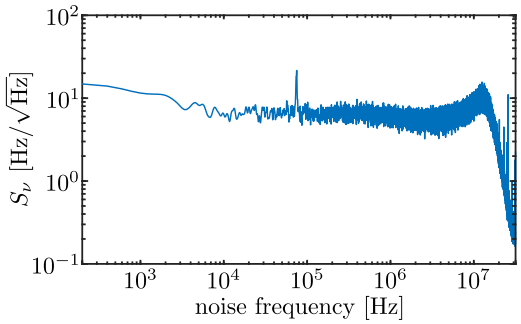

Fig. 4. Frequency noise spectral density of the laser system as measured with a HighFinesse® Linewidth Analyzer.

3. Frequency noise spectral density

To demonstrate the high passive stability of our monolithic FFPCs, we perform the analysis of the frequency noise spectral density (FNSD), S_ν, of the error signal under different lock conditions (see main text Sec. 4.3). For this purpose, we measure the noise spectral density of the locked error signal using a spectrum analyser. The noise amplitude is then converted to the frequency noise of the cavity resonance by the slope of the PDH-error signal to obtain S_ν. Fig. 5 shows the FNSD for three FFPCs for a sub-Hertz (blue) and a few kHz (red curve) locking bandwidths. The gray trace is the off-resonance (detection) noise limit. To gain insight about the noise distribution, we also show the integrated rms frequency noise, $\Delta\nu_{\mathrm{rms}}$, in the inset for the respective FFPCs. The results of these measurements are summarized in Tab. 1. $\Delta\nu_{\mathrm{rms}}$ is only slightly increased while locking even at sub-Hertz locking bandwidth as compared to higher locking bandwidths, testifying the high passive stability of the FFPCs.

As shown in the insets of Fig. 5, $\Delta\nu_{\mathrm{rms}}$ is increased close to the 50 Hz, due to the coupling to the electrical line frequency, and at around 1 kHz by ambient acoustic noise.. The latter is confirmed in a separate measurement using a microphone sensor.

Table 1. Frequency noise for the three FFPCs.

Property	Half slot FFPC	Full slot FFPC	Triple slot FFPC
$\Delta\nu_{rms}$ (800 mHz LBW)	0.48 MHz	0.73 MHz	1.19 MHz
$\Delta\nu_{rms}$ (minimum)	0.37 MHz*	0.40 MHz#	0.64 MHz§
$\Delta\nu_{rms}$ noise floor	0.31 MHz	0.25 MHz	0.24 MHz

* 3.7 kHz LBW ; # 3.7 kHz LBW ; § 1.7 kHz LBW; $\Delta\nu_{rms}$ - integrated for 10 Hz – 1 MHz

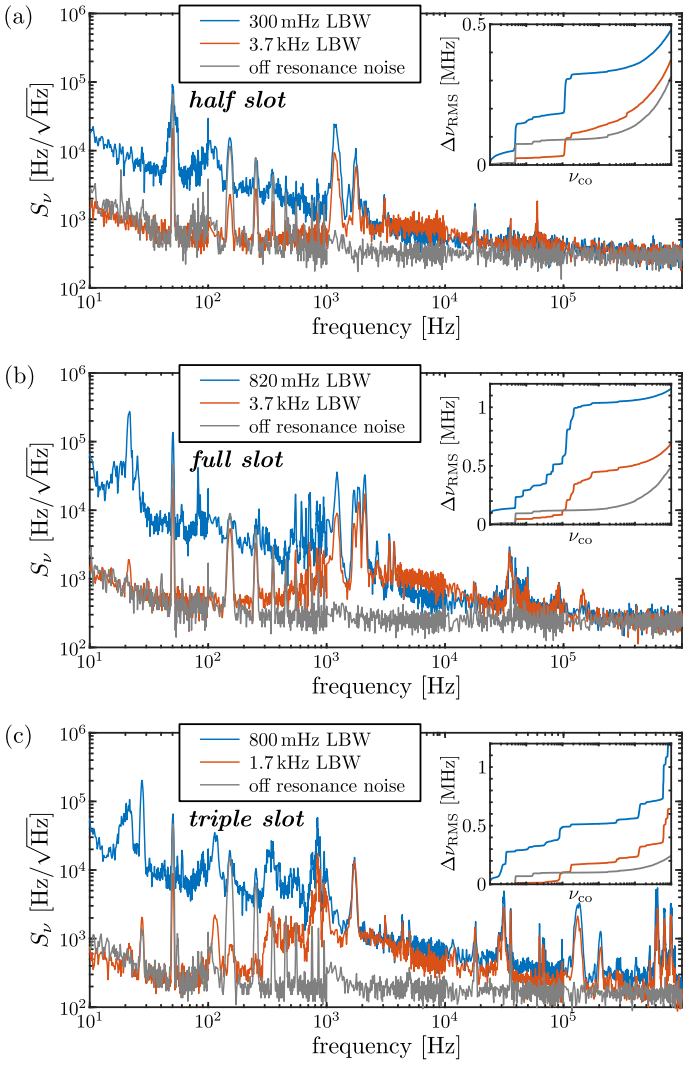

Fig. 5. Frequency noise spectral density (FNSD) of an FFPC locked to a narrow linewidth laser. Inset shows the cumulative rms frequency noise vs ν_{co}, where ν_{co} is the rms integration cut-off frequency. a) half slot , b) full slot and c) triple slot FFPC cases for different locking bandwidths.

4. Finite-element modeling and noise spectral density calculation

To estimate the influence of the mechanical modes of the devices on the frequency stability, we performed finite element simulations (COMSOL [1]). The obtained mode frequencies and displacement fields are used to calculate the optomechanical coupling of the mechanical modes to the optical cavity mode. The resulting frequency noise spectral density of the optical mode is then retrieved via the fluctuation-dissipation theorem.

4.1. COMSOL simulations

For an overview of the basic modes and their coupling, a symmetrized geometry is simulated first, see Fig. 6 (a). Here, short silica fiber pieces (diameter=125 µm) that terminate with the end of the piezo-element (1 mm × 1 mm × 10 mm, triple slot piezo width: 2 mm) are used. The silica ferrule (1.25 mm × 1.25 mm × 10 mm) holds the fibers in a fitting bore. The fiber ends are separated in the center by the approximate cavity length. The material of the piezo-element is lead zirconate titanate. Its mechanical properties are simplified by only using the Y11 component of the Young's modulus (63 GPa). The model does not include damping, hence the simulated eigenmode frequencies are real valued. The displacement fields and eigenfrequencies of two of the lowest order mechanical modes that couple to the optical resonator for all three designs are shown in Fig. 6 (b). These modes occur in all simulated geometries and correspond to a bending and stretching mode of the devices.

From the displacement fields $\mathbf{u}(x, y, z)$ as retrieved in the simulations the effective mass m_{eff} of each mechanical mode [2] for all geometries is calculated as

$$m_{\mathrm{eff}} = \frac{\int_V \mathrm{d}V\ \rho(x, y, z) \cdot |\mathbf{u}(x, y, z)|^2}{\max_V(|\mathbf{u}(x, y, z)|^2)}, \tag{1}$$

with V the full simulation volume and $\rho(x, y, z)$ the local density at position (x, y, z). The zero point motion x_{zpm} of each of the modes is then calculated using $x_{\mathrm{zpm}} = \sqrt{\hbar/2m_{\mathrm{eff}}\Omega_{\mathrm{m}}}$, with Ω_{m} the simulated angular eigenfrequency of the respective mechanical mode. The vacuum optomechanical coupling rates g_0 are then extracted by

$$g_0 = G \cdot x_{\mathrm{zpm}} \cdot \left(\frac{u_{z,\mathrm{mirror},1}}{\max_V(|\mathbf{u}|)} - \frac{u_{z,\mathrm{mirror},2}}{\max_V(|\mathbf{u}|)} \right), \tag{2}$$

where $G = -2\pi\nu_0/L_{\mathrm{cavity}}$ is the optomechanical coupling to the optical mode at frequency ν_0 and L_{cavity} the cavity length (here fixed at 95 µm). The factor $u_{z,\mathrm{mirror},i}/\max_V(|\mathbf{u}|)$ scales the displacement along the cavity axis of each of the mirrors i to the full maximum displacement of the mode, since the calculated x_{zpm} refers to the maximum displacement position [2].

4.2. Noise spectral density modeling

The optomechanical coupling strengths and eigenfrequencies of the mechanical modes as retrieved from the simulations are used to calculate the expected frequency noise of the optical mode due to the thermal excitation of the mechanical resonances. This is achieved by applying the fluctuation-dissipation theorem to obtain the spectral density of displacement fluctuations of the mechanical modes of the devices. These are then coupled to the optical mode frequency by the respective optomechanical coupling strengths [3]. The resulting single-sided frequency noise spectral density $S_\nu(f)$ of the optical mode from a single mechanical mode at Ω_{m} is thereby given as

$$S_\nu(f)^2 = 2 \cdot \frac{S_{\omega\omega}(\Omega)}{4\pi^2} \approx \frac{2g_0^2}{4\pi^2} \cdot \frac{2\Omega_m}{\hbar} \cdot \frac{2\Gamma_{\mathrm{m}} k_{\mathrm{B}} T}{(\Omega^2 - \Omega_{\mathrm{m}}^2)^2 + \Gamma_{\mathrm{m}}^2\Omega^2}. \tag{3}$$

Where the noise frequency is $f = \Omega/2\pi$, k_{B} the Boltzmann constant, T the temperature of the device and $\Gamma_{\mathrm{m}}/2\pi$ the linewidth of the mechanical resonance. The rms frequency fluctuation

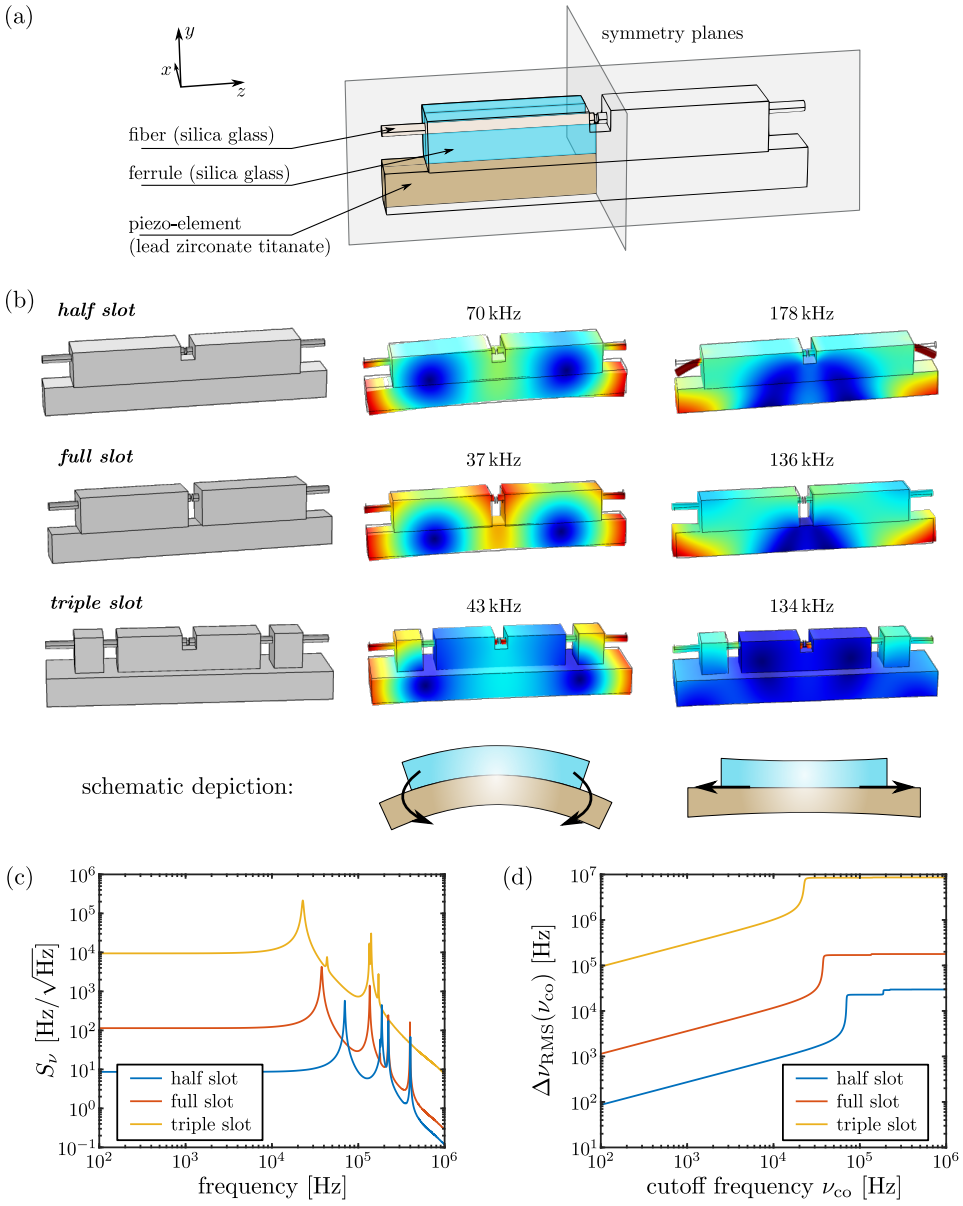

Fig. 6. Simulation of the mechanical modes of the symmetrized FFPC geometry. (a) shows the different components and symmetry planes of the simulated devices. The columns in (b) show the geometry and the displacement fields of two typical mechanical modes occurring in all geometries. They are labelled with the respective simulated eigenfrequency. The last row in (b) shows a schematic depiction of the device displacement of the two modes. The frequency noise spectral densities for the three different geometries as expected from the thermal fluctuations of the simulated mechanical modes are plotted in (c). This can be translated into a rms frequency fluctuation by integrating up to a certain cutoff frequency as shown in (d). The linewidth of the mechanical modes was arbitrarily fixed at $\Gamma/2\pi = 1$ kHz for visualization. The noise for the triple slot FFPC in (c) and (d) is overestimated, since the motion of the fibers in the center ferrule part is for simplicity modelled as a free movement, which cannot accurately describe the sliding of the fibers.

up to a certain cutoff frequency ν_{co} is then calculated as $\sqrt{\int_0^{\nu_{\mathrm{co}}} \mathrm{d}\nu\, |S_\nu(f)|^2}$. Alternatively, the contributions of the mechanical modes can be used to obtain the rms frequency fluctuations by $\sqrt{\sum_j 2g_{0,j}^2 \langle n_{\mathrm{j}} \rangle}/2\pi$ [3], with $g_{0,j}$ being the vacuum optomechanical coupling strength and $\langle n_{\mathrm{j}} \rangle$ the expectation value of the mechanical mode occupancy ($k_{\mathrm{B}}T/\hbar\Omega_{\mathrm{m},j}$ for $k_{\mathrm{B}}T \gg \hbar\Omega_{\mathrm{m},j}$) of the jth mode. Figure 6 (c) and (d) show the resulting modeled frequency noise spectral densities of the optical mode and the corresponding integrated rms fluctuation for the three designs. Since the finite-element simulations did not take damping effects into account, the linewidth of the mechanical modes was arbitrarily fixed at $\Gamma_{\mathrm{m}}/2\pi = 1\,\mathrm{kHz}$ for all modes in the preliminary analysis. Note that the full ($\nu_{\mathrm{co}} \to \infty$) rms frequency fluctuation does not depend on Γ_{m}.

For the final combination of measured frequency noise spectral densities and simulations, the frequencies and linewidths of the mechanical modes of the exemplarily chosen full slot FFPC were fitted in the measured spectrum. The fitted noise peaks were then attributed to mechanical modes in the simulations at close-by frequencies. To get a final estimate of the noise caused by the thermal fluctuations, $S_\nu(f)$ was calculated using the fitted mode frequencies and linewidths together with the vacuum optomechanical coupling strengths of the attributed mechanical modes from the simulations. Thereby slight shifts of the mechanical mode frequencies caused by deviations from idealized geometry are captured. Also, the corresponding linewidths are extracted without the necessity to include mechanical damping in the finite-element simulations.

4.3. Effect of structure asymmetries

In order to get a more realistic prediction of the expected frequency noise, a detailed model without the symmetry simplification and including some more properties of the final devices and some common imperfections was set up exemplarily for the full slot FFPC geometry, see Fig. 7. The introduced asymmetry causes more modes to couple to the optical resonance, e.g. sideward bending modes, whose coupling would otherwise be prevented by the symmetry. The longer fiber parts and the included silver glue pads at the bottom of the piezo cause the mechanical mode frequencies to slightly shift. More importantly, also the optomechanical coupling of the mechanical modes changes since the effective mass and the displacement fields are altered. For the model presented here, slightly smaller coupling strengths and thereby also smaller rms noise was retrieved from the more realistic model. Some pronounced noise peaks in the spectrum slightly below 100 kHz appear, which can also be found in the measured noise spectra. The final combination of measurement and simulation as presented in the main text used the more detailed model with the parameters $(\delta_{\mathrm{longitudinal}}, \delta_{\mathrm{lateral}}, \theta_{\mathrm{tilt}}) = (1.9\,\mathrm{mm}, 0.05\,\mathrm{mm}, 0.2^\circ)$ and a height of 0.5 mm for the glue pads on the bottom of the piezo (see Fig. 7).

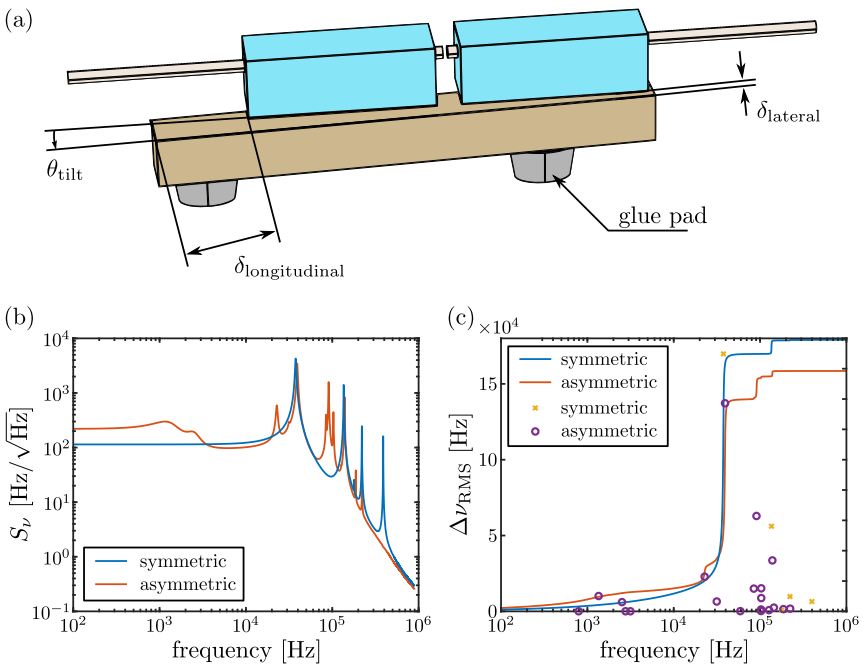

Fig. 7. Effect of asymmetries on the modeled spectra and rms noise. (a) shows an exaggerated sketch of the asymmetries and imperfections that were included in the finite-element simulations. To get a more realistic estimate of the spectrum the parameters were chosen as $(\delta_{\mathrm{longitudinal}}, \delta_{\mathrm{lateral}}, \theta_{\mathrm{tilt}}) = (1.9\,\mathrm{mm}, 0.15\,\mathrm{mm}, 0.3°)$ here. In addition the length of the fiber pieces outside the ferrule was increased to 5 mm and the conductive glue points were included as silver pads at the bottom of the device (glue height: 0.7 mm, width fitting to the piezo-element). The comparison of the resulting spectra (exemplary $\Gamma_{\mathrm{m},j}/2\pi = 1\,\mathrm{kHz}$) is plotted in (b). The asymmetry leads to a number of weakly coupled additional resonances as well as to a small reduction of the optomechanical coupling strengths, which results in a smaller estimate for the rms fluctuations in (c). Aside the integrated spectra also the separated contribution of each individual mode j to the rms noise $\sqrt{2g_{0,j}^2\langle n_j\rangle}/2\pi$ for both the original, simplified symmetric and for the more realistic asymmetric model are indicated.

5. Other FFPC properties

5.1. Thermal tuning

In addition to the fast piezo tuning as described in the main text, thermal tuning can also be used to change the cavity length. Fig. 8 shows the change in the cavity resonance frequency as the ambient temperature of single slot FFPC is varied. Here the FFPC is placed inside a thermally isolated box which has a Peltier element and a sensor to change and stabilize the temperature to a desired value. From the slope of the curve, the measured temperature tunability is 8 GHz/K.

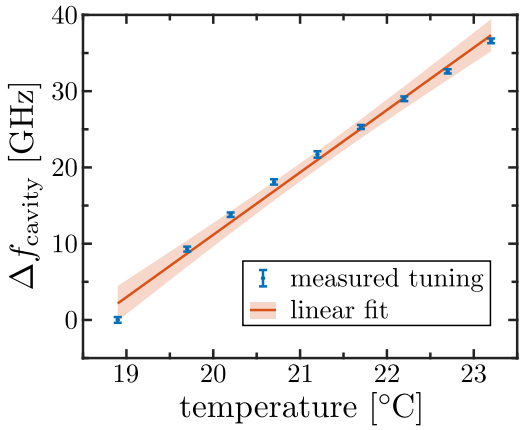

Fig. 8. Thermal tuning of a temperature controlled and isolated Half slot FFPC. Tunability of 8 GHz/K is obtained from the measurement shown here.

References

1. COMSOL AB, "COMSOL Multiphysics® v. 5.2," www.comsol.com. Stockholm, Sweden.
2. M. Aspelmeyer, T. J. Kippenberg, and F. Marquardt, *Cavity optomechanics: nano-and micromechanical resonators interacting with light* (Springer, 2014).
3. M. Gorodetksy, A. Schliesser, G. Anetsberger, S. Deleglise, and T. J. Kippenberg, "Determination of the vacuum optomechanical coupling rate using frequency noise calibration," Opt. express **18**, 23236–23246 (2010).